Three Dimensional Molecular Imaging for Lignocellulosic Materials

P.W. Bohn (Notre Dame) and J.V. Sweedler (Illinois at Urbana-Champaign)

Final Report - DE FG02 07ER64497

The development of high efficiency, inexpensive processing protocols to render biomass components into fermentable substrates for the sequential processing of cell wall components into fuels and important feedstocks for the biorefinery of the future is a key goal of the national roadmap for renewable energy. Furthermore, the development of such protocols depends critically on detailed knowledge of the spatial and temporal infiltration of reagents designed to remove and separate the phenylpropenoid heteropolymer (lignin) from the processable sugar components sequestered in the rigid cell walls of plants. A detailed chemical and structural understanding of this pre-enzymatic processing in space and time was the focus of this program. We worked to develop new imaging strategies that produce real-time molecular speciation information *in situ*; extract sub-surface information about the effects of processing; and follow the spatial and temporal characteristics of the molecular species in the matrix and correlate this complex profile with saccharification. These technical objectives were addressed through the pursuit of three specific aims.

Specific Aim 1: Develop correlated optical and mass spectrometric imaging approaches for sub-surface imaging of LCMs in different states of processing. To realize this specific aim we propose: (a) to develop a new tool for sub-surface imaging utilizing second harmonic generation (SH-OCT) from the phenylpropenoid components of the lignin to generate contrast. (b) to develop secondary ion mass spectrometric approaches for spatially-resolved and depth-profiling. Data acquired by SH-OCT *in situ* will be used (c) to guide *ex situ* SIMS depth-resolved imaging of specific fragments of the phenylpropenoid backbone.

Specific Aim 2: Develop surface optical and mass spectrometric measures of lignin-hemicellulose-cellulose degradation at specific processing stages. (a) Optical measurements will exploit Raman imaging to acquire information about linkages among sugar units to follow the course of saccharification, and (b) mass spectrometric imaging will utilize matrix assisted laser desorption/ionization (MALDI) mass spectrometry (MS) and SIMS imaging to acquire molecular weight distributions of degradation products as a function of processing at the surface.

Specific Aim 3: Develop schemes to correlate *in situ* optical (Raman and SH-OCT) and mass spectrometric (SIMS and MALDI MS) information to generate depth-resolved maps of chemical information as a function of spatial position and processing time. (a) Concentrate on lignin in order to understand the manner in which degradation products form and the temporal profile of lignin degradation. (b) Compare the progress of delignification to the disruption of the pectin cross-linked cellulose microfibril network at specific locations.

Developments described below are organized according to specific aim.

Specific Aims 1 and 2

Mass Spectrometry (MS) approaches to characterize lignocellulosic materials. Efforts to further the potential of the large perennial grass *Miscanthus x giganteus* as a biofuel feedstock would be

aided by the ability to image the chemical species present during the fuel production process. Toward this end, two mass spectrometry imaging (MSI) approaches were investigated here—laser desorption/ionization mass spectrometry (LDI-MS) and secondary ion mass spectrometry (SIMS). With SIMS imaging, the distribution of small molecular and fragment ions can be imaged with higher spatial resolution, while with LDI-MS, larger molecules, like peptides and proteins, can be imaged at lower spatial resolution. Therefore, to achieve optimal biological imaging and maximize the chemical information recovered from a single sample section, a combination of these two MSI methods is preferred.

As a first step, cross sections of *Miscanthus* were subjected to a variety of sample preparation methods to optimize conditions for MSI. For LDI-MS, a thin metal coating (2 nm thick Au) provided high quality signals of saccharide-related ions. The traditional matrix-assisted laser desorption/ionization matrix, 2,5-dihydroxybenzoic acid, also showed high efficiency for the desorption of saccharide-related ions. In contrast, with α-cyano-4-hydroxycinnamic acid matrix, these ions were nearly absent in the mass spectra. Direct laser ablation of untreated *Miscanthus* sections was also performed. High resolution images, where the fine structure of the vascular bundle could be clearly visualized, were obtained using SIMS. Because this work was performed simultaneously with our initial instrumental development efforts, the SIMS results were obtained using a PHI TRIFT III TOF-SIMS instrument (Physical Electronics, Chanhassen, MN) equipped with a gold liquid metal ion source operating at 22 keV. The SIMS instrument was partially supported by the DOE grants DE-FG02-07ER46453 and DE-FG02-07ER46471.

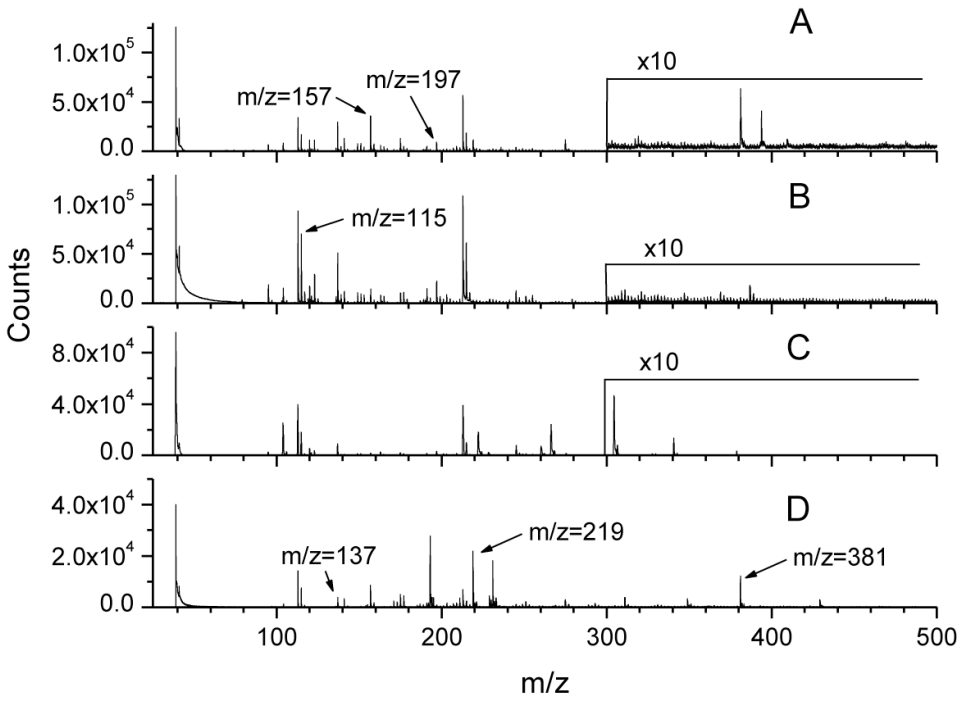

Figure 1. LDI mass spectra of *Miscanthus* cross sections from: (A) Au-coated section, (B) ITO slide, (C) CHCA-coated and (D) DHB-coated section. The y-axis scale is magnified ten-fold as indicated to highlight low intensity peaks.

Although coating the sections with a nanometer thick Au layer can greatly enhance the quality of SIMS images, the coating had limited effect on secondary ion signal enhancement. Using the optimized mass spectrometry approaches described here, information on the spatial distribution of several saccharides was obtained, with details provided below.

Miscanthus contains ~20% lignin. The phenyl structure in lignin absorbs ultraviolet laser light and thus, can potentially act as a self-matrix for direct desorption/ionization. Therefore, direct laser ablation of *Miscanthus* cross sections, without adding matrix, was evaluated first. In order to overcome sample charging during MS analysis, the samples were placed on an ITO slide. To further enhance signal, we also evaluated the use of a thin metal coating and its effect on spectral quality by depositing a 2 nm thick Au layer over the sample. Lastly, we also tested two conventional MALDI matrix coatings—DHB and CHCA.

Mass spectra obtained from direct laser ablation of *Miscanthus* cross sections showed a number of ions detected in the mass range below 500 Da (Fig. 1B); larger fragments from cellulose or lignin were not detected. The same phenomena were observed after coating the sections with Au, CHCA or DHB (Fig. 1A, C and D). Close comparison of the mass spectra obtained from the ITO (Fig. 1B) and Au-coated slides (Fig. 1A) showed the spectra were similar, except for the intensities of several saccharide-related ions at m/z = 219 ($C_6H_{12}O_6K^+$) and m/z = 381 ($C_{11}H_{22}O_{11}K^+$). The intensities of these two ions increased more than five-fold with Au-coating, thus indicating that Au coating reduces surface charging and may act as a matrix to enhance analyte ionization. The highest intensities for saccharide-related ions came from the DHB-coated samples (Fig. 1D). The intensities of ions at m/z = 219 and 381 were two-fold higher than from the Au-coated section (and ten-fold higher than with direct LDI), suggesting DHB is more efficient for the ionization of sugar-related ions. When CHCA was used as the matrix, most of the ions detected were fragments or clusters of CHCA; signals corresponding to the two saccharide ions were not detectable. While Au and DHB coating showed enhanced signal from saccharide-related ions, none of these sample preparation methods showed signal enhancement of the larger lignin and cellulose-related ions, including large fragment ions from cellulose.

Besides the detection and characterization of compounds, MSI provides distribution maps of the detected analytes. For example, images of strong sugar signals (m/z = 219 and 381) can be observed from the DHB-coated section (Fig. 2). The signals were stronger from the rim and vascular bundle region of the plant. Sugar ion images from the Au-coated section showed a similar distribution, but the signal intensities were lower, resulting in images with reduced contrast. Images of these ions from direct LDI were even weaker, but the vascular bundle structure of the plant tissue was still visible. From the CHCA-coated section, only a few randomly distributed spots were observed. Thus, for the imaging of sugar-related ions, both Au and DHB coating provide good results. The advantage of Au coating is that the sample preparation procedure is simpler.

The application of different matrices on varying substrates was found to introduce interferences at different masses. This is particularly relevant when analyte ions with the same nominal mass as the matrix ions show different distributions after the treatment procedures. For example, when Au was used as the sole matrix, m/z = 197 can mostly be attributed to Au^+ ions. As seen in Fig. 2, the signals were stronger at, but not limited to, the periphery. To eliminate interference from

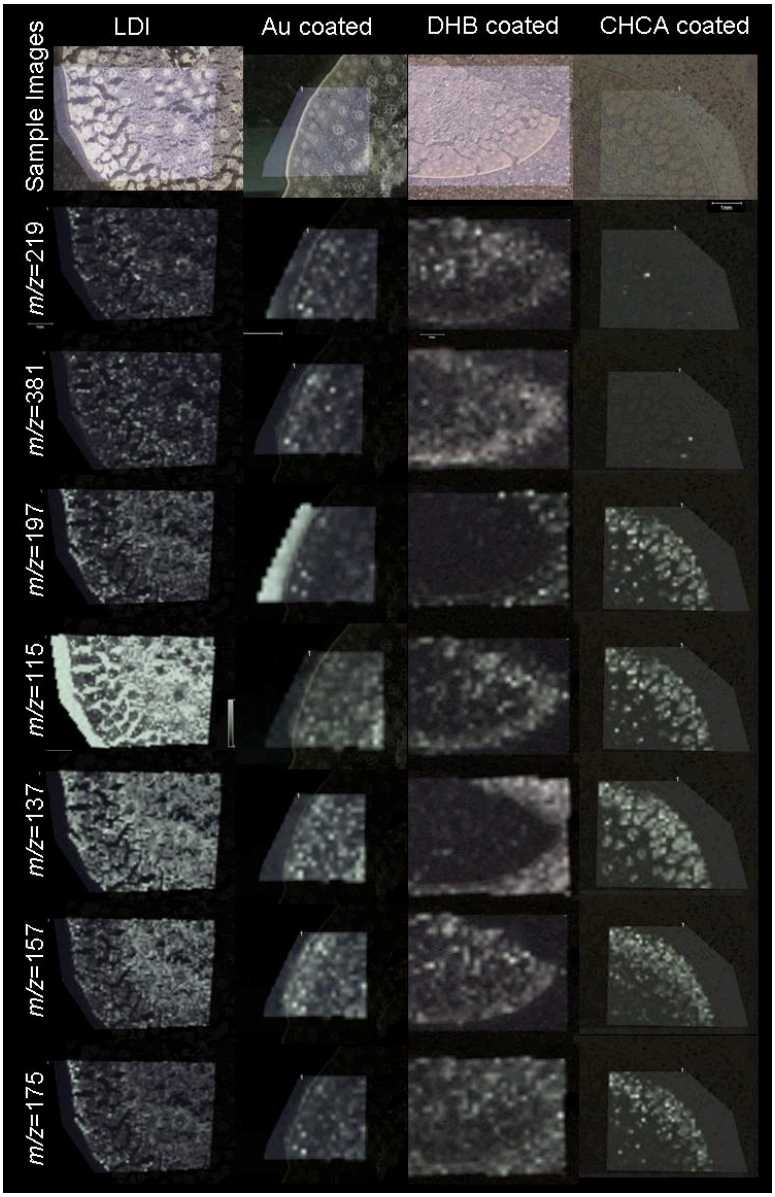

Figure 2. LDI-MS images of selected ions (rows) *vs.* different sample preparation conditions (columns). Scale bar: 1 mm.

Au^+ matrix ions, an image of ions at *m/z* = 197 was obtained by direct LDI, *i.e.* without Au. Most of the signals were from the plant tissue itself, and the distribution resembled that of other saccharide-related ions. The identities of these ions were tentatively assigned to $C_6H_{13}O_7^+$, which is a fragment ion of saccharide. Thus, the Au coating interferes with the detection of native ions at *m/z* = 197. Since both the DHB- and CHCA-coated sections were also coated with a 1 nm Au layer to reduce surface charging, it was expected that signal from the Au coating would dominate the region surrounding the plant tissue section. However, this was only observed on the DHB-coated section, indicating that CHCA suppresses interference from the Au coating.

Another example of matrix- or substrate-induced interference was observed at *m/z* = 115 (Fig. 2). When ITO was used as substrate, In^+ ions at *m/z* = 115 came mostly from the ITO substrate. In the image, a strong signal from the region surrounding the plant section can be observed. While on other samples, ions at this mass were assigned to $^{39}K^{41}KCl^+$ and $K_2{}^{37}Cl^+$. The localization of these ions was mostly confined to the plant section.

DHB has a fragment ion at *m/z* = 137 ($C_7H_5O_3^+$). From the DHB-coated section, most of the ions at *m/z* = 137 were from the substrate region (Fig. 2). When other matrices or substrates, besides DHB, were used these interferences were eliminated. The remaining *m/z* = 137 signals have been tentatively assigned to $C_8H_9O_2^+$, a fragment ion of lignin; these were detected exclusively from the plant itself. Another ion with similar distribution was observed at *m/z* = 175, assigned to

$C_8H_8O_2K^+$, the potassium adduct ion of the same lignin fragment. One ion that showed a ubiquitous presence in the plant section, regardless of the sample preparation method used, was *m/z* = 157. The identity of this ion was tentatively assigned to $C_6H_{13}N_4O^+$ or $C_6H_7NO_4^+$, perhaps an amino acid-related ion. In summary, for LDI imaging, no single sample preparation method provides complete coverage of the ions of interest. A combination of different matrices is needed to maximize the chemical information gleaned while minimizing matrix interference.

SIMS experiments were performed on both native plant tissue sections and Au-coated sections.

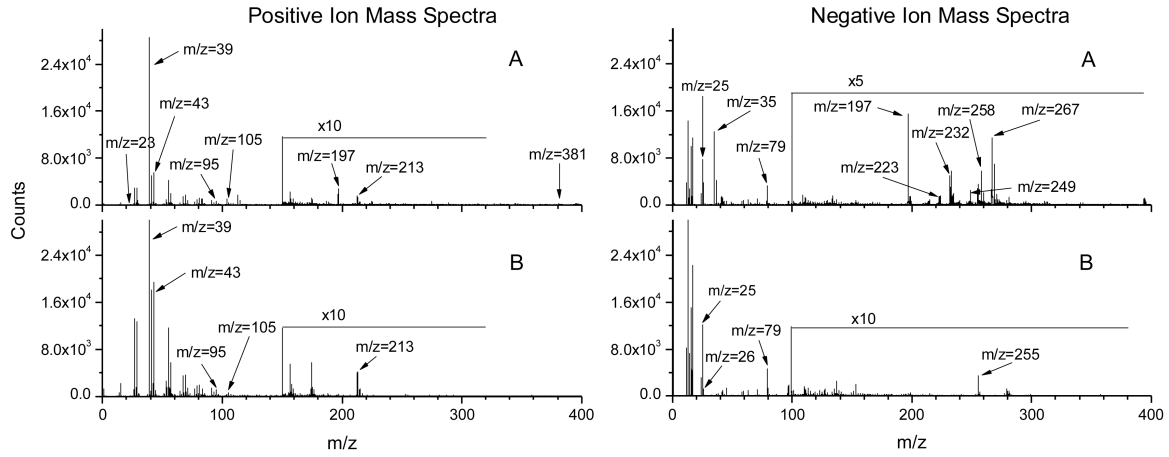

Figure 3. SIMS positive (*left*) and negative (*right*) ion mass spectra of *Miscanthus* cross sections from: (A) Au-coated sections, (B) native sections.

Mass spectra of the plant sections are shown in Fig. 3. Surprisingly, in the positive ion spectra, the Au coating did not produce significant signal enhancement. The intensities of most of the ions remained the same or even decreased after Au coating under similar mass spectrometric conditions. However, the section without Au coating did exhibit charge build-up during SIMS analysis due to the insulating nature of the tissue. This effect can be reduced by using charge compensation in the mass spectrometer, which was found to produce mass spectra of comparable quality to those from Au-coated sections. In the negative ion mass spectra, the Au coating introduced more interference than signal enhancement. The mass spectrum was dominated by Au chloride and cyanide adduct ions in the mass range of 200–300 amu (Fig. 3), such ions include: *m/z* = 223 ($AuCN^-$), *m/z* = 232 ($AuCl^-$), *m/z* = 249 ($AuCN_2^-$), *m/z* = 258 ($AuClCN^-$), *m/z* = 267 ($AuCl_2^-$), *etc*. These Au adduct ions greatly affected the ability to observe other ions.

As seen in Figs. 4 and 5, SIMS imaging of Au-coated and non-coated *Miscanthus* cross sections showed the fine structure of the plant. The cell walls and vascular bundles can be clearly observed, especially from the Au-coated sections. In contrast, with LDI imaging, the vascular bundle is represented by only a few pixels (Fig. 2). Moreover, images from the Au-coated sections were sharper than the corresponding images from non-coated sections, especially in the positive ion images. Taken together, the Au coating process enhanced the quality of the images, but failed to improve secondary ion yield.

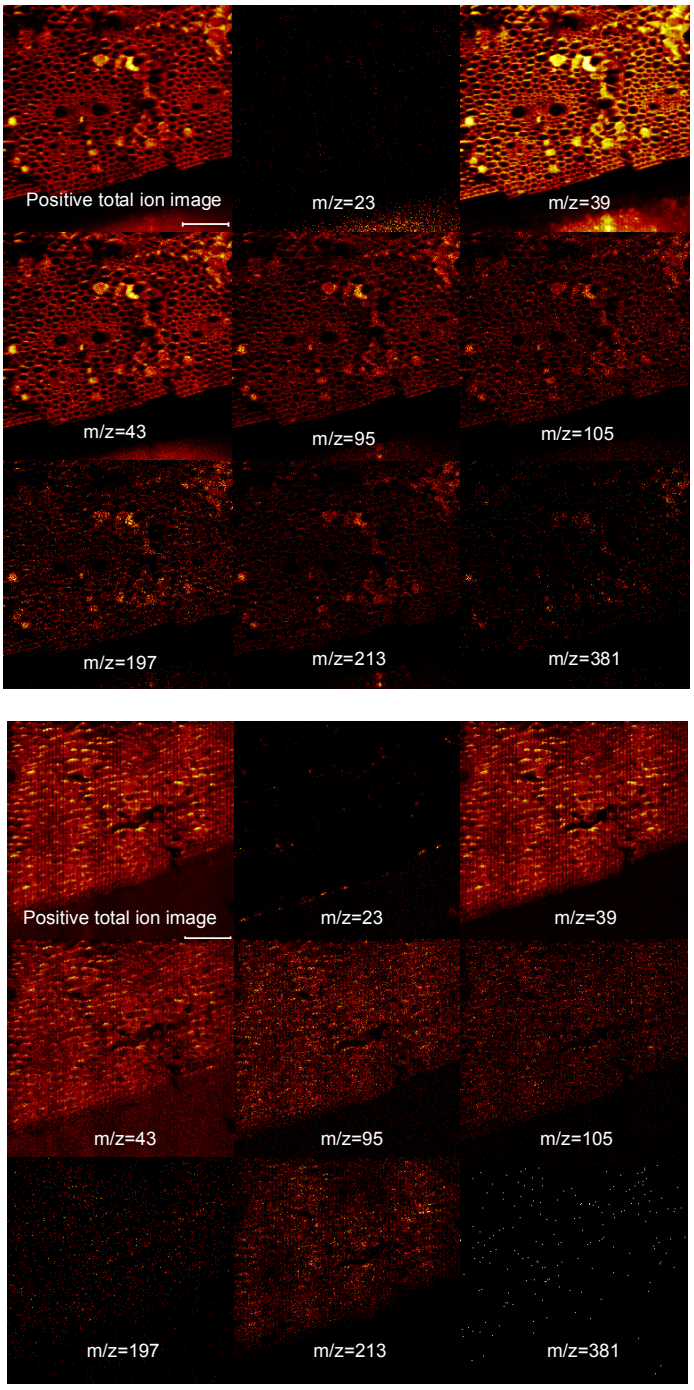

Figure 4. Positive ion SIMS images of *Miscanthus* cross sections showing both total positive ions and various *m/z* values: top panel, Au-coated section; bottom panel, non-coated section. Scale bar: 100 μm.

The most abundant positive ion observed in the spectra from both the coated and non-coated sections was potassium at *m/z* = 39 (Fig. 3). In the images shown in Fig. 4, K^+ showed ubiquitous distribution across both sections. Sodium ions at *m/z* = 23, in contrast, were barely detected from

the sections. On the Au-coated section, most of the Na^+ came from the substrate, while on the non-coated section, Na^+ ions were mostly detected at the sample-substrate interface. $C_3H_7^+$ at *m/z* = 43, representing fragment ions of organic species arising from lignin, cellulose or surface

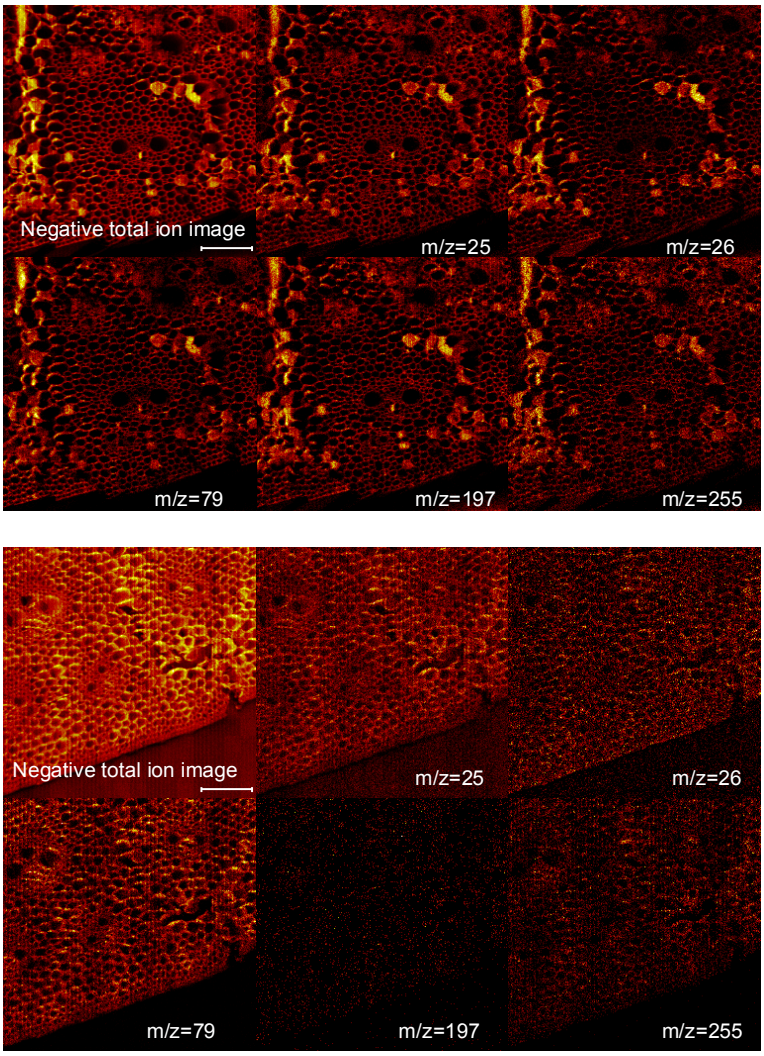

Figure 5. Negative ion SIMS images of *Miscanthus* cross sections showing both total negative ions and various *m/z* values: top panel, Au-coated section; bottom panel, non-coated section. Scale bar: 100 μm.

contaminants, was also universally detected. The images of ions at *m/z* = 43 showed contribution from both the plant section and the substrate, but the images from the plant regions resembled that of the K^+. Fragment ions at *m/z* = 95 ($C_6H_5OH_2^+$) were tentatively assigned to lignin, and those at *m/z* = 105 ($C_4H_9O_3^+$) (assigned to cellulose based on the same ion being observed from a cellulose standard) showed similar distributions, as expected, from colocalization and intermingling of lignin and cellulose in the plant cell wall. Spatial distribution of the secondary ion signal of Au^+ at *m/z* = 197 from the Au-coated section resembled that of the total ion image. The non-coated section showed only weak signal at this mass, the intensity being too low to generate a clear image. Ions at *m/z* = 213, which were also detected with high intensity from LDI

experiments, were observed throughout the plant section. In contrast, signals were weaker from the vascular bundle region. Saccharide-related ions at *m/z* = 381 ($C_{12}H_{22}O_{11}K^+$) were detected from the Au-coated section, but only at low intensity. The distribution of these ions was similar to *m/z* = 213 in the Au-coated section, but the signal intensity was too weak to provide a secondary ion image in the non-coated section.

The non-coated section displayed higher quality images in negative ion mode than in positive (Fig. 5). The images were sharper and the vascular bundle structure was clearly visible. Ions with *m/z* = 25 were mostly C_2H^-, arising from organic species on the sample surface. Images from the Au-coated and non-coated samples both showed uniform distribution of these ions across the whole section. CN^- ions at *m/z* = 26 were mostly derived from amino acids and other nitrogen-containing species. Signals were weaker from the vascular bundles of the sections, indicating reduced amino acid concentration in those regions. The image of phosphate ion (PO_3^-) at *m/z* = 79 was very similar to the total ion image, indicating that phosphate exists ubiquitously across the plant. Au^- ions were detected at *m/z* = 197 from the Au-coated section. From the non-coated section, a weak signal was observed at this mass. The distribution map showed most of the ions were still from the plant section, indicating that the Au coating interferes with detection of ions at *m/z* = 197, similar to what was observed in the positive ion and LDI images. Lignin-related ions at *m/z* = 255 ($C_{16}H_{15}O_3^-$, $C_6H_5C_3H_6OC_6H_4COO^-$) had an image similar to the positive lignin fragment ions at *m/z* = 95 (Fig. 5). They both showed uniform distribution across the tissue section. In summary, SIMS imaging can reveal the densely packed cell wall structure of the *Miscanthus* stem. Most of the secondary ions detected were fragment ions of lignin and cellulose. Unlike LDI-MS experiments, SIMS produced weak signals from saccharide-related ions. Au coating can greatly enhance the quality of SIMS images, especially positive ion images.

The efficacy of both LDI-MS and SIMS for the imaging of *Miscanthus* cross sections was investigated using a variety of sample preparation methods. For LDI-MS imaging, no single sample preparation method provided both complete chemical information and spatial distribution of analytes in the sample. Most of the matrices tested enhanced detection of saccharide-related ions, although several approaches induced interference at certain masses. Thus, in LDI-MS, a combination of two or more sample preparation methods should be used to obtain coverage of a broad range of compounds. None of the matrices tested showed an enhancement of larger fragment ions from cellulose. Coating the sample with Au is the simplest method and provides abundant information with the least interference. Thus, for time-limited analyses, Au coating is the method of choice. In the LDI images, signals from saccharide- and lignin-related ions were more emphasized in the rim and vascular bundle regions. In contrast, the higher spatial resolution SIMS images of that region revealed densely packed cell wall structures. SIMS images also showed colocalization of lignin and cellulose. Coating the tissue sections with Au enhanced the quality of SIMS images, especially in the positive ion mode. In the negative ion mode, the Au coating interfered with the detection of some species. The enhancement in secondary ion yield with a thin layer metal coating is not significant for the plant tissues tested here. Surprisingly, for several masses, the yields decreased after Au coating.

In addition, several experiments were implemented that use these protocols to analyze LCMs subjected to a range of pretreatment methods, as well as during the various stages of the biofuel production process, allowing us to monitor and evaluate the efficiency of such methods.

The last area of MS-development of Aim 1 included the design and development of a prototype secondary ionization mass spectrometer with a C_{60} cluster ion source for imaging lignocellulosic materials, with a schematic of the instrument shown in Fig. 6. This construction and development effort worked out well and the unique hybrid instrument is illustrated below.

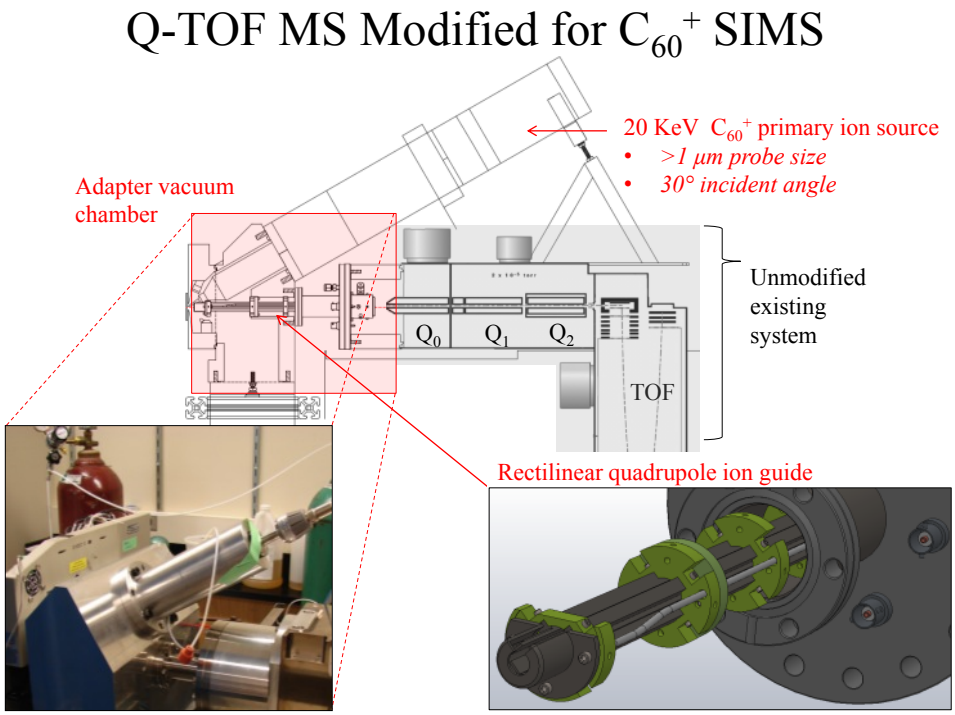

Figure 6. Prototype hybrid LDI/SIMS instrument created during this project that involved modifying a commercial Q-TOF MS to add a C_{60} ion source.

Current work involves optimizing its performance for a range of samples as well as improving its depth profiling and spatial resolution capabilities. While this sub-aim proved to be more challenging than expected, the creation of a unique LDI/MALDI instrument with high resolution and tandem-MS capabilities will be of interest in a number of follow-up projects related to DOE missions.

Confocal Raman Imaging. Alkaline pretreatment of lignocellulosic materials (LCM) has been reported to remove lignin and partially remove hemicellulose, thus rendering the remaining cellulose more accessible to enzymatic digestion. In this work, confocal Raman microscopy (CRM) was employed to investigate the structural and chemical changes in model LCM upon NaOH treatment. *Miscanthus x giganteus*, which is a tall perennial grass and is regarded as a potential energy crop for conversion to either fuel or chemicals, was used as a model LCM. Thin sections of *miscanthus* were treated using different concentrations of NaOH at various temperatures and for different lengths of time. Then, confocal Raman imaging of *miscanthus* sections was carried out in water at room temperature using a confocal Raman microscopy (Alpha 300R, WITec GmbH, Germany), equipped with a doubled Nd:YAG (λ=532 nm) excitation laser and a 60x water immersion objective from Nikon (NA=1.0). The spatial

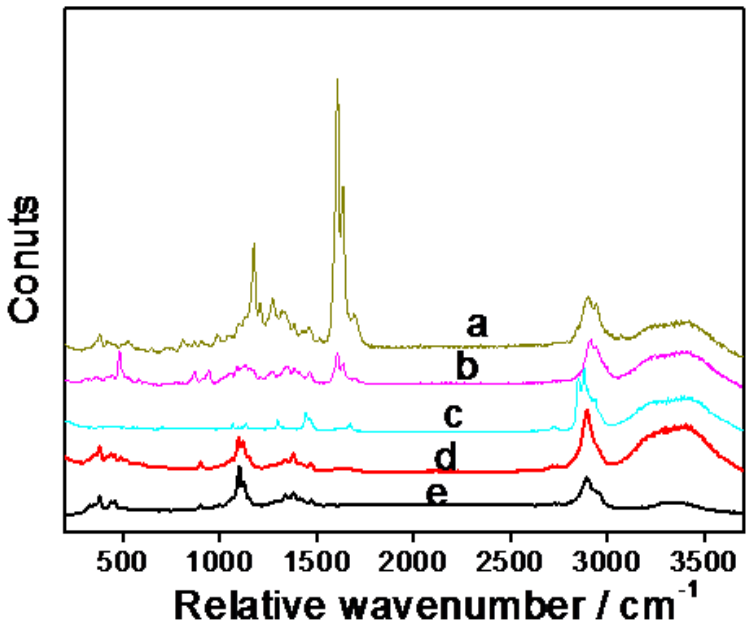

Figure 7. Raman spectra acquired from NaOH-treated as well as from raw *miscanthus*. (a) parenchyma cell wall in raw *miscanthus*; (b) globular structure in raw *miscanthus*; (c) extracted solid in the NaOH treated *miscanthus*; (d) parenchyma cell wall in the NaOH treated *miscanthus* (10% NaOH, T = 50 °C, 20 h); (e) pure cellulose powder as reference (acquired in air).

resolution of the current Raman system is estimated to be < 500 nm.

Figure 7 shows typical Raman spectra acquired from raw, as well as from NaOH treated, *miscanthus*. Figure 7a is the average Raman spectra from the cell wall of untreated *miscanthus*. Raman band assignments for *miscanthus* were based on the previous reports about other plants. Briefly, the bands at 378 and 1096 cm^{-1} are assigned to cellulose, while those at 1601, 1629, and 3066 cm^{-1} are from lignin. Bands in the C-H stretching region at and 2894 and 2940 cm^{-1} are primarily assigned to cellulose and lignin, respectively. From Figure 7a, it is apparent that both cellulose and lignin are present in the

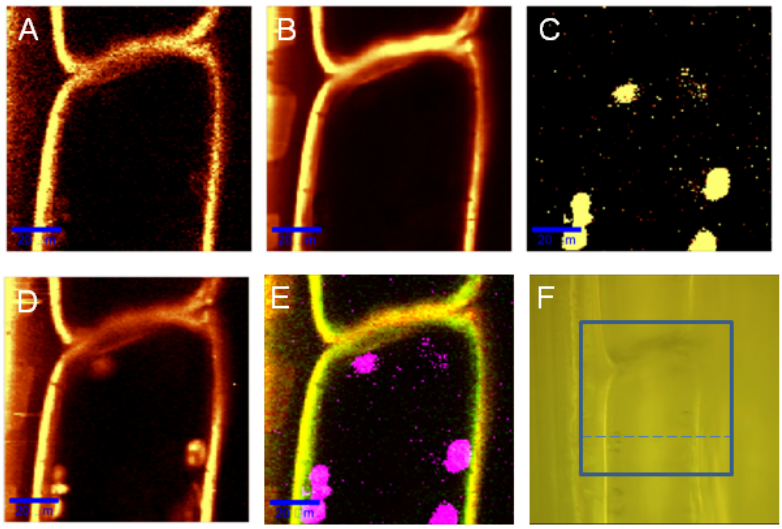

Figure 8. Raman images showing the distribution of various components raw *miscanthus* in the *x-y* direction (*i.e.* lateral mapping). (A) Cellulose, 345-390 cm^{-1}; (B) Lignin, 1550-1650 cm^{-1}; (C) Lignin-hemicelluloses complex, 460-500 cm^{-1}; (D) All organic components 2820-3000 cm^{-1}; (E) Color-coded image, where red represents lignin, green for cellulose and pink for Lignin-hemicellulose complex; (F) Optical refraction image of *miscanthus* longitudinal section.

parenchymal cell wall of raw *miscanthus*. The Raman bands for hemicellulose, which is another main component of *miscanthus*, were not visible. This phenomenon is most likely explained by a combination of the fact that the hemicellulose in *miscanthus* is amorphous, and thus exhibits weak Raman response, and that it is present in relatively low abundance, such that it is masked by the Raman signal of crystalline cellulose.

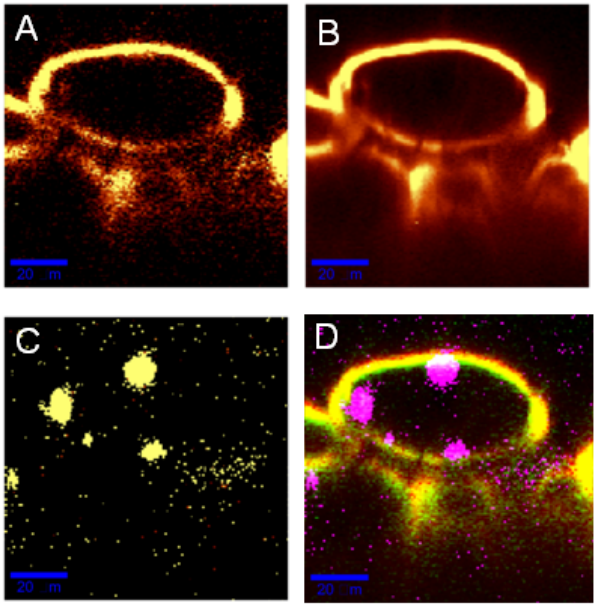

Figure 9. Raman images showing the distribution of various components in raw *miscanthus* in the *x-z* direction (*i.e.* depth profiling). (A) Cellulose, 345-390 cm^{-1}; (B) Lignin, 1550-1650 cm^{-1}; (C) Lignin-hemicellulose complex, 460-500 cm^{-1}; (D) Color-coded images, where red represents lignin, green for cellulose and pink for lignin-hemicellulose complex. Scale bar, 20 μm.

In raw *miscanthus*, characteristic globular features were also found located inside the parenchyma cell (see the pink elements in Figs. 8E and 9D), whose Raman spectrum is shown as Figure 7b. Besides the characteristic lignin band at 1601 cm^{-1}, a sharp band is observed at 478 cm^{-1}, which can be assigned to hemicellulose. Therefore, the globular structures contain both lignin and hemicellulose, but there is little evidence for cellulose in them.

As mentioned above, lignin can be removed by NaOH treatment. Figure 7d shows the Raman spectrum of a *miscanthus* sample treated with 10% aqueous NaOH solution at T = 50 °C for 20 h. After NaOH treatment the lignin band at 1601 cm^{-1} is largely eliminated, indicating that the lignin was extracted out completely from *miscanthus* as expected. Furthermore, when comparing Fig. 7d to the pure cellulose Raman spectrum (Fig. 7e), one can see that the spectra are almost identical, indicating that the parenchyma cell wall consists almost entirely of cellulose (see Fig. 10), and the morphology of cellulose fibers remained unchanged by this NaOH treatment. This is in good agreement with previous reports that find that the transformation of cellulose I to cellulose II occurs only at higher concentration of NaOH (>16%).

In the NaOH treated *miscanthus*, one can also see some globular structures as well (see Fig. 10). However, the Raman spectrum of these structures in the NaOH-treated samples (as shown in Figure 7c) clearly demonstrates that they are different from the lignin-hemicellulose complex in the raw *miscanthus*. Particularly, a sharp shoulder band at 2845 cm^{-1} can be observed in Fig. 7c, which was assigned to a wax substance in the literature. Therefore, our results suggest that some wax was extracted from *miscanthus*, which was not soluble in NaOH, and thus remained inside the cell.

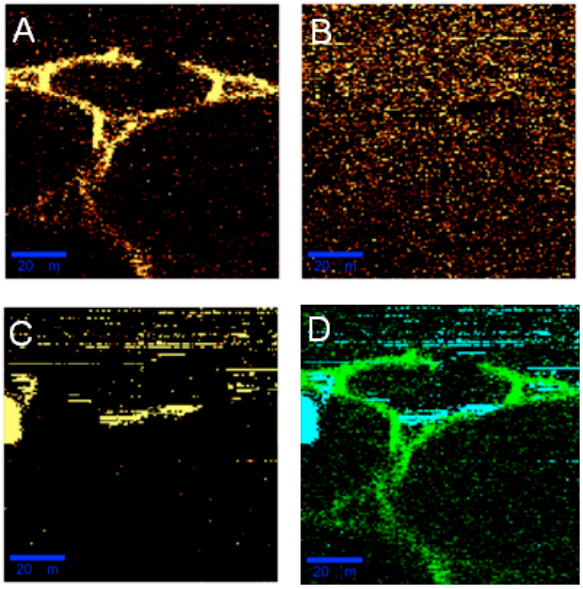

Figure 10. Raman images showing the distribution of various components in the NaOH treated *miscanthus* in the *x-z* direction. (A) Cellulose, 345-390 cm^{-1}; (B) Lignin, 1550-1650 cm^{-1}; (C) Wax, 2820-2860 cm^{-1}; (D) Color-coded images, where green represents cellulose and light blue for wax. Scale bar, 20 μm.

NaOH treatment conditions, including NaOH concentration, treatment temperature, treatment time, were all varied to reveal their influence on *miscanthus* delignification. Figure 11 shows a depth profile of a partly delignified *miscanthus* (10% NaOH, T = 80 °C, 4 h). From Figure 11c, it is apparent that some lignin aggregates (red part) on the upper side of the cell wall, likely resulting from redeposition of extracted lignin onto the cell wall. When comparing the Raman spectra from the upper and lower parts of the cell wall (Fig. 11d), the intensity of the lignin band at 1601cm^{-1} is much higher in the upper part than that for cellulose at 1096 cm^{-1}, however, in the lower part of cell wall, the cellulose band is stronger. This result suggests that lignin indeed moved to the upper part, *i.e.* to the outside portion of the processed cell wall. The section analysis in Fig. 11e exhibited the same trend.

To conclude this section, confocal Raman microscopy was successfully utilized to follow both structural and chemical changes in *miscanthus* parenchyma cells upon NaOH treatment. Using the powerful combination of spectral and spatial information it is possible to begin to build 3D models of composition in response to realistic processing conditions and to visualize critically important outcomes of the processing such as delignification.

Specific Aim 3

The conversion of LCMs into biofuels typically involves three steps: (1) pretreatment, which allows for the separation of cellulose and/or hemicelluloses from lignin; (2) saccharification, or the enzymatic hydrolysis of cellulose/hemicellulose into monomeric sugars; and (3) fermentation, which converts sugars into ethanol using yeast. The first step, pretreatment, is critical, since saccharification cannot proceed in the presence of a significant amount of lignin. Thus, a great deal of effort is being put into the optimization of pretreatment processes in order to reduce total LCM biorefining costs. Efficient pretreatment can improve the enzymatic hydrolysis of cellulose by disrupting the cell wall structure, reducing the crystallinity of

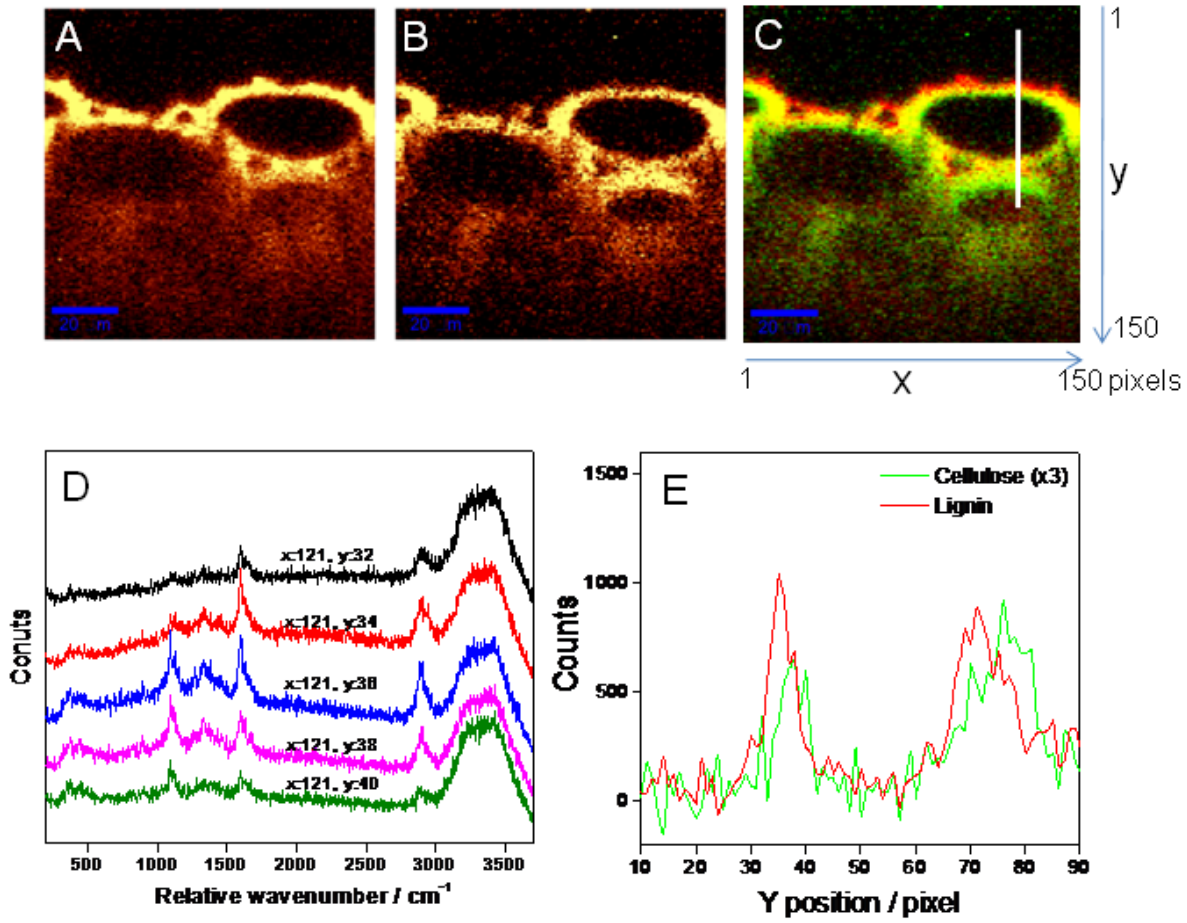

Figure 11. Raman images showing the distribution of various components in NaOH-treated *miscanthus* in the *x-z* direction. (A) Cellulose via integration over 345-390cm^{-1}; (B) Lignin via integration over 1550-1650cm^{-1}; (C) Color-coded images, where red represents lignin, green for cellulose; (D) Raman spectra at various positions of cell wall as indicated in (C); E) Comparison of cellulose and lignin Raman intensity along the line in (C). Scale bar, 20 μm.

cellulose, and increasing the accessible area. Nearly all studies of pretreatment protocols have had to rely on composite evaluative data, such as cellulose yield, to guide development. Clearly, the ability to directly visualize the molecular nature of LCMs as a function of pretreatment protocols would be enormously beneficial. To this end, spatially correlated Raman scattering and secondary ion mass spectrometry (SIMS) imaging, as described in the preceding section were combined to assess *Miscanthus x giganteus* from the same samples at the same locations. Specifically, confocal Raman microscopy (CRM) and SIMS imaging were used to correlate optical and mass spectrometric data and generate chemical information as a function of spatial position and processing time.

CRM and SIMS were combined with LDI-MS to investigate the structural and chemical information in a model LCM, *Miscanthus x giganteus*. The approach used to correlate spatial positions among the three different imaging modalities is shown in Figure 12. Briefly, the

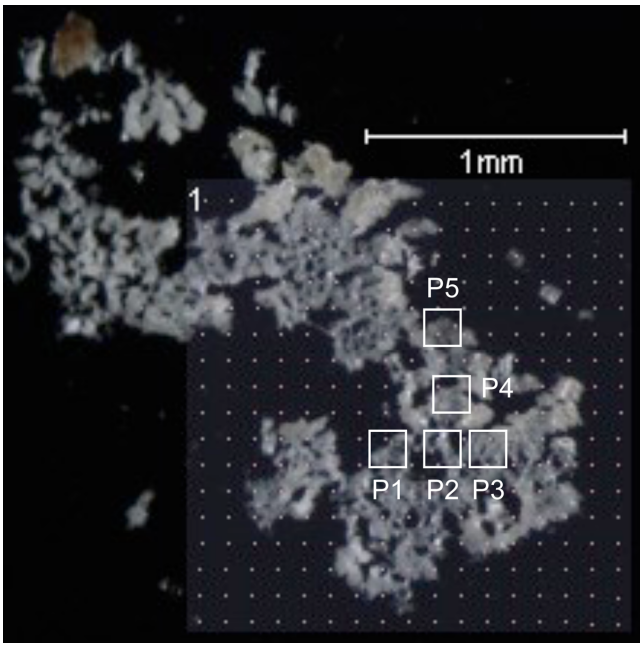

Figure 12. Overlay of an optical image, the LDI-MS grid, and five ROIs for SIMS and confocal Raman imaging for a *Miscanthus* sample.

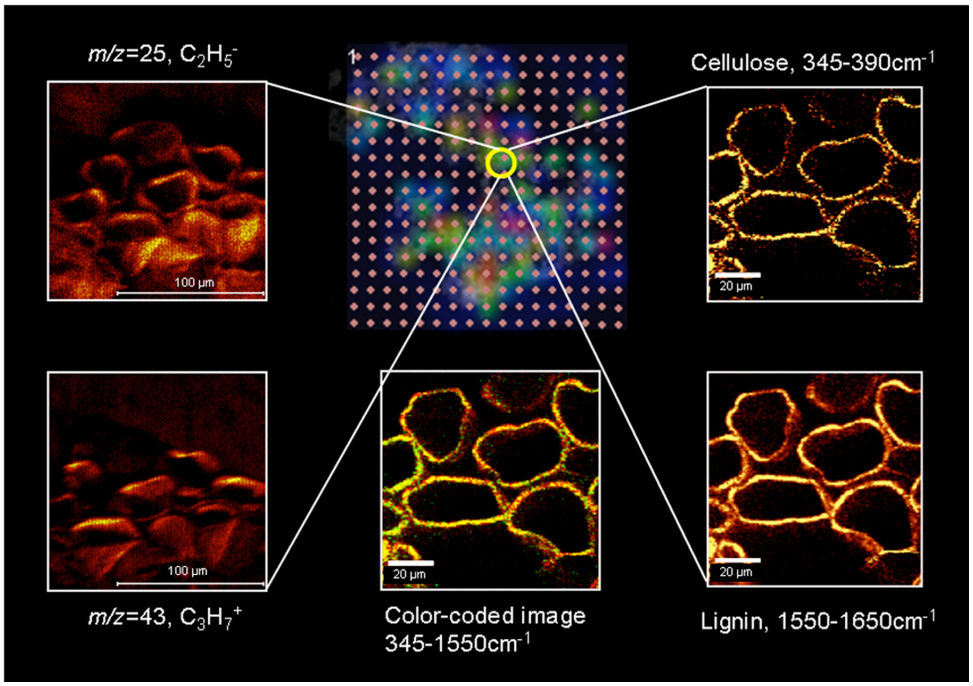

Figure 13. Overview of the LDI-MS/SIMS/CRM spatial correlation strategy. The LDI-MS grid (*center top*) is color-coded, corresponding to the intensity of $m/z = 45$ ions obtained by laser desorption-ionization excitation spots on 100 µm centers. The yellow circle highlights the spot where high resolution imaging was performed by both negative ($m/z = 25$, C_2H^-, *top left*) and positive ($m/z = 43$, $C_3H_7^+$, *bottom left*) ion SIMS, as well as CRM, characterized by the cellulose band, 345 – 390 cm^{-1} (*top right*), and the lignin band, 1550 – 1650 cm^{-1} (*bottom right*). (*Bottom center*) Composite CRM image combining information from both cellulose (green) and lignin (yellow) bands.

irregular shape of the *Miscanthus* samples was imaged optically and used to provide an *in situ* map, with readily identifiable landmarks to serve as registration aids when transferring samples between laboratories. Figure 12 shows that the LDI mass spectra were acquired from a grid of points, these data being obtained after high resolution imaging by CRM and SIMS to allow larger areas to be probed for higher molecular weight compounds.

Figure 13 outlines the overall strategy used. First, CRM imaging was used to analyze the *Miscanthus* cross-sections in an ambient environment. Characteristic bands of cellulose (345 – 390 cm^{-1}) and lignin (1550 – 1650 cm^{-1}) were monitored. The CRM images, as well as optical microscopic images, provided landmark registration for SIMS analysis, where the distributions of both negative (m/z = 25) and positive (m/z = 43) ions were imaged. Since both CRM and SIMS only imaged a small region of the sample (150 μm × 150 μm), a larger sample area was profiled by LDI-MS, with a spatial resolution of 100 μm. The LDI-MS image of m/z = 45 is shown in Figure 13 as well.

The *Miscanthus* samples in vacuum (SIMS) exhibited no significant structural change when compared to those in air (CRM and optical images). Previous CRM images of *Miscanthus* were acquired in water to reduce unwanted autofluorescence background. However, with improved CRM methodology, the background was reduced, thereby reducing the need for water immersion. Raman images of *Miscanthus* are clearly dominated by the cell wall, where cellulose and lignin are colocated. Raman bands characteristic of hemicelluloses, another major component of cell walls, are not visible in Fig. 13, either because the hemicelluloses in *Miscanthus* cell walls are amorphous and thus exhibit weak Raman response, or because their abundance is relatively low, so that they are masked by the Raman signal of crystalline cellulose.

In order to elucidate the chemical nature of *Miscanthus*, SIMS experiments were carried out at the identical positions at which the CRM images were acquired. Total secondary ion images

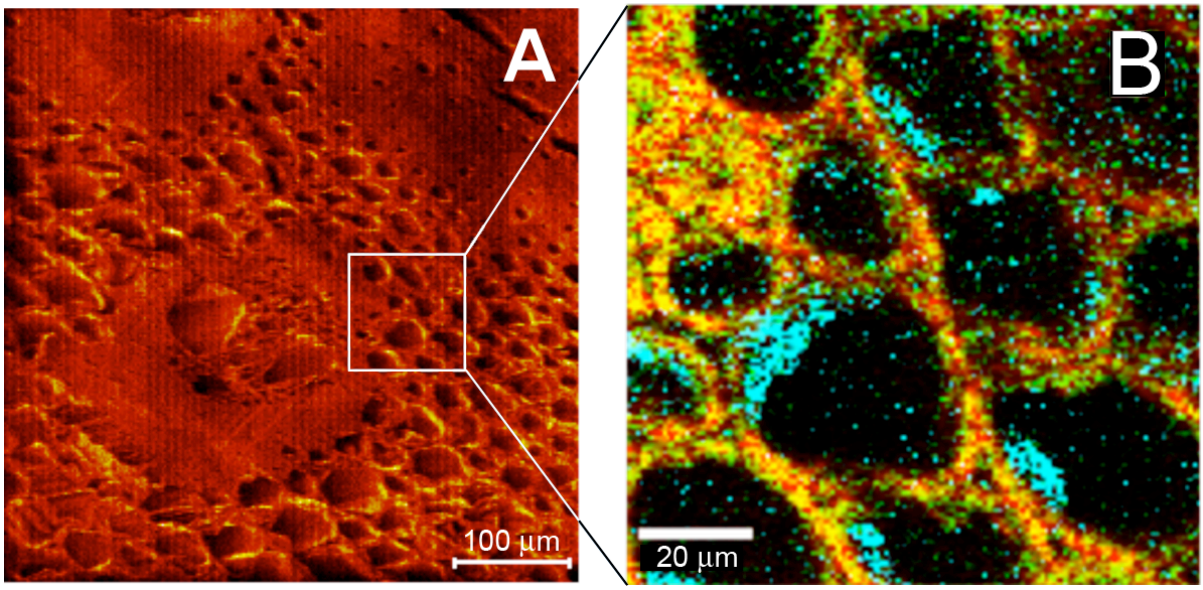

Figure 14. **(A)** Total negative ion SIMS image of the vascular bundle region. **(B)** Color-coded CRM image of the boxed ROI in panel A; red = lignin, 1550 – 1650 cm^{-1}, green = cellulose, 345 – 390 cm^{-1}, and blue = lignin-hemicellulose (460 – 500 cm^{-1}) complex.

(Figure 14A) show a well-preserved cell wall structure. These images also correlate well with the Raman images, indicating that the sample preparation method employed here was well-suited for the analysis of plant samples using SIMS and Raman microscopy. The negative total ion image (Figure 14A) showed better contrast than the positive total image, primarily due to increased secondary ion intensity from hydrogen in the negative mode. The distribution maps of fragment ions corresponding to lignin (*m/z* 95, $C_6H_5OH_2^+$) and cellulose (*m/z* 105, $C_4H_9O_3^+$) generally overlap with each other, which is in agreement with the Raman images. The intensity of hemicellulose fragment ions, *m/z* 133 ($C_5H_9O_4^+$), was weak, making localization of hemicellulose by SIMS difficult.

To overcome the low signal-intensity issue, a region of interest (ROI) analysis of the SIMS data was performed in order to compare the total spectrum, obtained from the accumulation of all secondary ions collected in the total ion image with a spectrum acquired from the region imaged by CRM and with an ROI on the interior of the cell. The spectra (not shown) from these two regions were essentially identical, indicating that the region imaged with CRM faithfully represented the overall chemical composition of *Miscanthus*. The second ROI overlapped with the globular structure highlighted in blue in Figure 14B, and was assigned to a hemicellulose-rich lignin complex. A comparison of the mass spectra between the overall structure and the hemicellulose-rich region shows that the intensities of two ions increased significantly: *m/z* 133 ($C_5H_9O_4^+$), a fragment ion from pentose, and *m/z* 181 ($C_6H_{12}O_6H^+$), assigned to either a hexose fragment ion or a pentose cluster ion. Pentose is the scaffold of hemicellulose; therefore, the increased signal intensity of pentose fragment ions from the globular structure from the interior of the cell confirms the tentative assignment made from the CRM image.

In summary, spatially correlated SIMS and Raman imaging were used to provide high quality, high resolution subcellular images of *Miscanthus* cross sections. Furthermore, the combination of information from the mass spectrometry and Raman scattering allows specific chemical assignments of observed structures, difficult to assign from either imaging approach alone and lays the foundation for subsequent heterocorrelated imaging experiments targeted at more challenging biological systems, such as the interacting plant-microbe systems relevant to the rhizosphere.

Publications – DEFG0207ER64497

Comparison of Sample Pretreatments for Laser Desorption Ionization and Secondary Ion Mass Spectrometry Imaging of Miscanthus x Giganteus, Z. Li, P.W. Bohn, J.V. Sweedler, Biores. Technol. 101, 2010, 5578–5585.

Spatial Correlation of Confocal Raman Scattering and Secondary Ion Mass Spectrometric Molecular Images of Lignocellulosic Materials, Z. Li, L-Q. Chu, J.V. Sweedler, P.W. Bohn, Anal. Chem. 82, 2010, 2608-2611.

Base-Induced Delignification of Miscanthus x Giganteus Studied by Three-Dimensional Confocal Raman Imaging, L-Q. Chu, R. Masyuko, J.V. Sweedler, P.W. Bohn, Biores. Technol. 101, 2010 , 4919–4925.